Journal of Harbin Engineering University
ISSN: 1006-7043

Vol 46 No. 1
January 2025

Development of a Drone Test Bench with a High-Precision Directional Force Measurement System for the Isolation of Thrust Forces of Individual Propellers of a Quadcopter

Edgard Siryle Tolo[1*], Anthony Muchiri[2], Jackson Njiri[2], Shohei Aoki[2]

1. Department of Mechanical and Mechatronic Engineering, Pan-African University, Institute for Basic Sciences, Technology and Innovation, Nairobi, 6200-00200.
2. Department of Mechatronic Engineering, Jomo Kenyatta University of Agriculture and Technology, Nairobi, 62000-00200.

Abstract

This paper presents the development of a directional force measurement system designed to evaluate the thrust of individual propellers on a quadcopter during flight. This direction of study was primarily motivated by the need to create a high-precision force measurement system, with the aim of paving the way for robust development and advancement of the local Unmanned Aerial Vehicles industry. Among its major features is its ability to successfully isolate measured forces of the combined quadcopter's propellers into individual propeller thrusts. To achieve this, the developed directional force measurement system encompasses an integrated system of four cross-force sensors. The separate readings of the four sensors, through a model derived from repeated calibration of the system, firstly, with known weights, and eventually a quadcopter in yaw, roll, pitch, and hover motions, yield the respective thrust values of each propeller. The system was installed on its designated frame and, in synergy with an accelerometer and a microcontroller, formed a physical drone test bed. This then facilitated the successful measurement of the forces generated by individual propellers. Data visualisation and collection were made possible via a website and a cloud database system, respectively, both in direct communication with the microcontroller and the sensors. The test data was then extracted and utilised to validate the model created.

Keywords: Force measurement system; drone test bed; load cells sensors; unmanned aerial vehicles (UAVs); mathematical modelling.

1. Introduction

Drones, also known as Unmanned Aerial Vehicles (UAVs), have become essential tools across various fields due to their ability to operate without a human pilot. Their applications range from wildlife monitoring [1–3] and rescue operations [4, 5] to public venue surveillance [6, 7], medical supply delivery [8, 9], field mapping and monitoring [10, 11], and even disinfection of zones in need of such procedures [12]. This rapid spread of drones into various fields has increasingly served as a significant driver towards adjustments (advancements) in their basic structure. These adjustments have consequently led to a significant surge in drone prices, making it challenging for low-income regions to adopt emerging technologies [13].

As drones evolve, they often integrate new mechanical and electrical components, resulting in heavier designs [14–16]. For instance, UAVs are now utilised as carriers for environmental sensors and cameras [17], while advancements in robotic manipulators have required their integration with drones to enhance mobility and agility. However, this integration presents challenges due to the under-actuated nature of UAVs, where they have fewer actuators than degrees of freedom, limiting their control capabilities. For example, quadrotor UAVs can control only four of their six degrees of freedom, with X and Y positions lacking direct control [18]. To address these limitations, researchers like Huang [18]. Are developing advanced manipulator systems for Vertical Take-Off and Landing (VTOL) aircraft. Additionally, studies from institutions such as the University of Pennsylvania [19] investigate navigation control and stability of hexacopter-based mobile robots to enhance their performance in diverse

environments [20]. Despite addressing weight issues, quadrotors still face challenges related to performance and stability during critical phases like lift-off and hovering. Valiga et al. [21], the increasing weight of drones due to new applications requires robust force monitoring systems to account for the forces and torques involved during operation. Monitoring parameters such as acceleration and orientation is crucial for adapting designs and improving efficiency in applications like disaster response and precision agriculture [22].

Accurate measurement of directional forces in UAVs remains a challenge due to the current system's inability to fully account for real-world aerodynamic variations that impact stability and performance [24].This research aims to fill a critical gap by developing a high-precision directional force measurement system that isolates individual propeller thrusts during flight. Integrated into a comprehensive drone test bed, this system will enable effective monitoring and optimisation of UAV performance, particularly for those with additional components. The goal is to enhance safety, design, control, and operational capabilities within UAV technology.

While existing force measurement systems have limitations regarding real-world aerodynamic variations, a comparative benchmark with current techniques could strengthen claims regarding the proposed system's superiority.

2. Objectives

The main objective of this study is to develop a drone test bed that can isolate and measure the directional force generated by the propellers of multirotor UAVs. In order to isolate and characterise this objective, the following specific objectives were identified:

1. To design and develop a test bed for drone flight parameters measurement.
2. To test and calibrate the test bed using force measurements from a commercial drone and blocks of known weight
3. To evaluate the performance of a drone by isolating force generated by individual propellers from those read from force sensors.

3. Materials and Methods

3.1 Measurement platform

The directional force measurement system comprises mechanical, electrical, software and control modules. These separate systems are then synergistically integrated to function as a common unit to realise a successful system capable of monitoring various drone parameters before they are declared fit for deployment into their respective production stages. This integrated system is briefly highlighted in this section in its separate modules.

The mechanical system comprises a mounting platform, four tension springs, and a square frame stand. The frame, constructed from 12.5*12.5*4 mm angle lines, stands at an overall dimension of 1000 mm*1000 mm. With holes across its widths' centre points, it successfully facilitates the rigid mounting of the four respective load cells, which interlink with the four tension springs to the mounting platform at the frame's centre. The mounting platform's elevation off the ground equals that of the frame stands (60mm). Its overall outer diameter is 700 mm, with its inner diameter standing at 300mm. This design improves both the mechanical performance and measurement accuracy, ensuring that the system remains stable, durable, and adaptable in various conditions. Autodesk Inventor designed the mechanical system. Physical fabrication was mainly achieved using conventional cutting and joining processes, such as hack sawing and arc welding, among others. The material for the frame was painted mild steel grade A-36; the mounting platform was aluminium 6063, whereas the tension springs were Music Wire ASTM A228. The complete assembly of the design and its fabricated physical are as in Figures 1 and Figure 2, respectively.

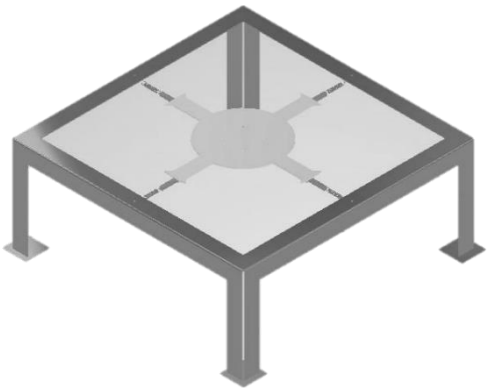

Figure 1. Drone Test Bed Design

Figure 2. Fabricated Drone Test Bed

3.2 Data capture system

The electrical and control modules comprised an accelerometer (9-axis MPU9250), a microcontroller (NODEMCU ESP32S), and four load cells (strain gauge force sensors). The 9-axis accelerometer was selected majorly owing to its possession of a trio of tri-axis magnetometer, gyroscope, and accelerometer. These features make it a 9-axis motion-tracking device that, in combination with a Digital Motion Processing Device (DMP), on-chip 9-axis motion fusion, and runtime calibration firmware, eliminates system-level integration, guaranteeing optimal motion performance. The NODEMCU ESP32S was selected due to it is Wi-Fi and Bluetooth capabilities that allow for seamless wireless communication, which is crucial for real-time sensor data transmission and reception to a visual interface (a website, in this scenario); just enough GPIO pins to accommodate all the necessary components (the four load cells and an accelerometer); ease of programming and installing both the hardware, and the visual display software interface; and a fast processor, which facilitates seamless data processing. The strain gauge load cells, on the other hand, were selected due to their precise ability to measure forces, deformation, pressure, and moments acting on solids [25]. This type of force sensors are basically transducers that convert forces into measurable electrical output by utilising the Wheatstone bridge, as shown in Figure 3, and an ADC converter or amplifier. The ADC converter is very vital as it is solely responsible for the conversion of analogue signals produced by load cells into digital forms readable by digital devices [26]. The HX711 amplifier was thus selected.

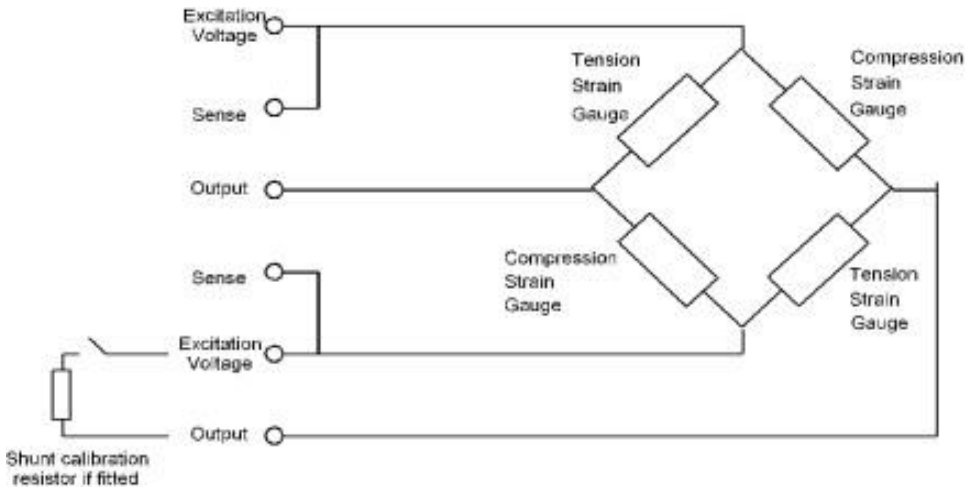

Figure 3. The Wheatstone bridge

The eventual synergistic integration of the modules above led to the realisation of a system capable of monitoring the various drone performance parameters (orientation, acceleration, attitude, and

directional forces/thrust of the individual propellers). To achieve this, the accelerometer and the four load cells take their respective readings and send them to the microcontroller. To facilitate user visualisation of these respective parameters, a visual interphase was designed in the form of a website. This was made possible by the presence of a database, which serves to store all the data collected by the sensors in real time. This respective data is then fetched and displayed to the visual interface in the form of tabulated cards and pictorial forms, as well as the progress bars within the cards and line graphs.

3.3 System Calibration

Calibration was conducted in two separate stages: individual calibration of each load cell and collective calibration. Ideally, the force sensors should display zero upon unloading the entire system. However, this is not always the case [27]. This is owed to the volatility of the Wheatstone bridge system upon continuous long periods of usage and, as such, tends to become prone to errors. This is scientifically attributed to the algebraic differences between the values indicated as sensor output against the actual measured values [26]. These errors arise from factors such as zero offset linearity, hysteresis, repeatability, non-repeatability, and temperature shift span and are graphically illustrated in Figure 4.

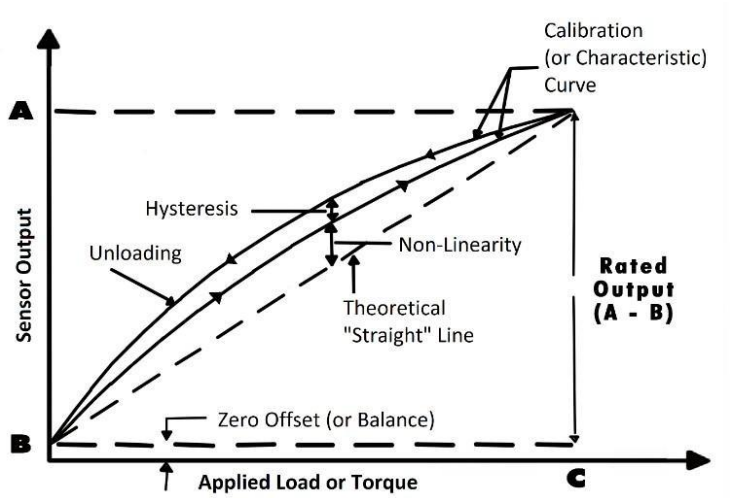

Figure 4. Graphical representation of calibration errors

To calibrate the load cells, two known weights of 1kg and 2kg were sequentially placed on the mounting platform. Twelve loading points were marked out on the measurement platform, as illustrated in Figure 5

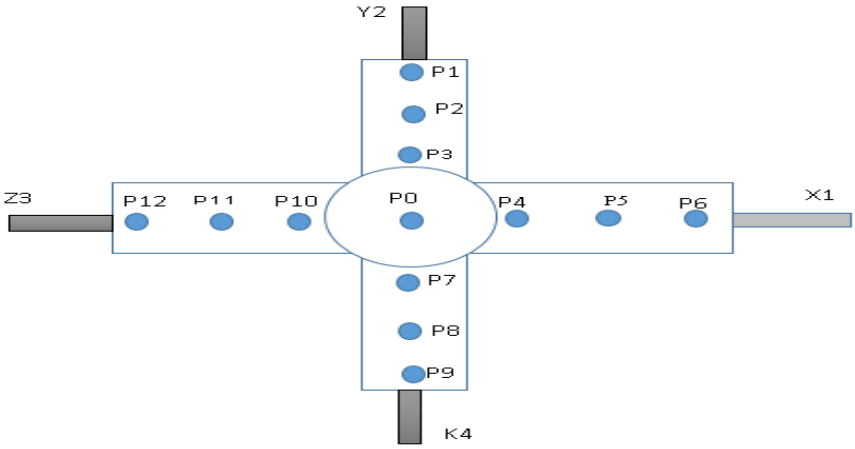

Figure 5. Loading Points on the test bed's mounting platform.

Each point was identified by a number and a coordinate position X (β) and y (α). Table 1 shows the point coordinates for the twelve measurement points:

Table 1: Point coordinates

	Po	P3	P4	P7	P10	P2	P5	P8	P11	P1	P6	P9	P12
X(β)mm	0	0	X	0	0	x	0	0	x	0	0	x	0
Y(α)mm	0	x	0	X	0	0	x	x	0	x	x	0	x

Point 0 was at the centre of the platform. P3, P7 and P10 were at X mm from the centre point. Other points are shown in Table 1. Each time a weight is applied, the load cell generates an output value, which is displayed on a serial monitor. This output reflects the load cell's response to the applied weight. After each measurement, the system is unloaded and then reloaded in a series of cycles numbered 1 to 10, during which data is collected for each load cell. Single-point measurements were done with the known weights being placed on P1 to P12. The measurement process is illustrated in Figure 6.

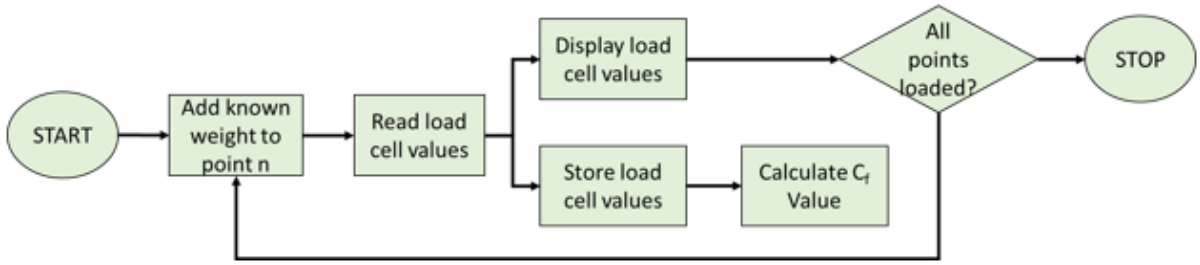

Figure 6. Calibration Sequence Chart

Double point loads were done in combinations shown in Table 2.

Table 2: Loading point summary

Type of Loading	**Loading Points**
Single Point Loads	P0, P1, P2, P3, P4, P5, P6, P7, P8, P9, P10, P11, P12.
Double Point Loads	P1-P9, P2-P8, P3-P7, P6-P12, P5-P11, P4-P10, P3-P4, P4-P7, P7-P10, P10-P3, P2-P5, P5-P8, P8-P11, P11-P2, P1-P6, P6-P9, P9-P12, P12-P1

A Calibration Factor (C_f) was determined to allow for the accurate conversion of future load cell readings into actual force measurements, ensuring reliable performance in various applications. This factor is the ratio between the average of the measured value (R) and the reference weight W and is expressed in Equation 1 [28]:

$$C_f = \frac{R}{W} \quad (1)$$

The recorded values from these cycles are compiled in Table 3:

Table 3. Calibration Values (kg)

	Mass kg	C_f Load Cell 1 g	C_f Load Cell 2 g	C_f Load Cell 3 g	C_f Load Cell 4 g	Total N
Cycle 1	1 kg	256.04	248.72	248.33	247.71	9.81
Cycle 2	1 kg	255.73	259.44	247.98	248.10	9.91
Cycle 3	1 kg	256.63	241.11	244.38	252.12	9.75
Cycle 4	1 kg	256.98	244.15	245.50	251.83	9.79

Cycle5	1 kg	256.66	242.24	246.08	251.55	9.78
Cycle 6	2 kg	505.06	486.03	495.44	500.46	19.48
Cycle 7	2 kg	504.39	481.68	494.30	501.18	19.44
Cycle 8	2 kg	505.26	482.66	493.53	501.05	19.44
Cycle 9	2 kg	503.54	484.25	493.19	500.52	19.44
Cycle 10	2 kg	502.13	485.19	492.74	500.73	19.44

3.4 Equation Formulation

The next step was to develop an equation that determines the load measured by the platform, regardless of its position. The variables from the previous measurements, namely the radius r and the point positions X (β) and Y (α), were used.

The calibration values from Table 3 show a linear relationship, even when plotted on a graph. A multi-linear Regression model would best suit modelling this data into an equation [29].

The model equation was determined as follows: From the general MLR equation (2) below and the training data collected in subsection 2.1, training of a fitting model equation was achieved using the relationship:

$$Y = B_0 + B_1X_1 + B_2X_2 + B_3X_3 + \ldots + B_PX_P + \epsilon \quad (2)$$

Where A is: $\begin{pmatrix} \sum(R)^2 & \sum R\beta & \sum R\alpha \\ \sum R\beta & \sum(\beta)^2 & \sum \beta\alpha \\ \sum R\alpha & \sum \beta\alpha & \sum(\alpha)^2 \end{pmatrix}$,

B is: $\begin{pmatrix} B1 \\ B2 \\ B3 \end{pmatrix}$, and C is : $\begin{pmatrix} \sum X_1Y \\ \sum X_2Y \\ \sum X_3Y \end{pmatrix}$.

However, the summations indicated here are not the actual sums obtained from the raw training data. From the raw summations, it was possible to obtain regression summations, which are then utilised in the derivation of a fit model. The regression summations necessary for calculating the coefficients in the multi-linear regression model were computed as detailed in Equations (5) (13). These values were used to derive the final model for isolating propeller thrusts as below.

$$\sum(R)^2 = \sum(R)^2 - \sum(R)^2/n \quad (5)$$
$$\sum(\beta)^2 = \sum(\beta)^2 - \sum(\beta)^2/n \quad (6)$$
$$\sum(\alpha)^2 = \sum(\alpha)^2 - \sum(\alpha)^2/n \quad (7)$$
$$\sum RY = \sum RY - (\sum R \sum Y)/n \quad (8)$$
$$\sum \beta Y = \sum \beta Y - (\sum \beta \sum Y)/n \quad (9)$$
$$\sum \alpha Y = \sum \alpha Y - (\sum \alpha \sum Y)/n \quad (10)$$
$$\sum R\beta = \sum R\beta - (\sum R \sum \beta)/n \quad (11)$$
$$\sum R\alpha = \sum R\alpha - (\sum R \sum \alpha)/n \quad (12)$$
$$\sum \beta\alpha = \sum \beta\alpha - (\sum \beta \sum \alpha)/n \quad (13)$$

To obtain B values (B_1, B_2, and B_3):

$$B = A^{-1}.C \quad (14)$$

B_0, however, is obtained separately through equation (15):

Where Y is the dependent variable, B_0 is the intercept, B_1, B_2, and B_3 are the regression coefficients representing the change in Y relative to a unit change in X_1, X_2, and X_3, respectively, and ϵ is the model's error (residual) term.

Having R, β, and α in place of X_1, X_2, and X_3, respectively, yields equation (3) below:

$$Y = B_0 + B_1R + B_2\beta + B_3\alpha + \epsilon \quad (3)$$

B_0, B_1, B_2, and B_3 are then obtained from equation (4) below:

AB= C (4)

$B_0 = \overline{Y} - B_1\overline{R} - B_2\overline{\beta} - B_3\overline{\alpha}$ (15)

The equations above, however, yield solutions to situations entailing multiple predictor variables and a single response variable. This paper, however, seeks to address a case with multiple (three) predictor variables (R, β, α) and multiple (four) response variables (x1, y2, z3, and k4). The four respective response variables are a percentage contribution of the four respective load cell values as distributed by the four respective propellers of the quadcopter together. In this scenario, Y is replaced by four distinct variables (x1, y2, z3, and k4), which represent percentage distributions to load cells 1, 2, 3, and 4, respectively, from each propeller. This modifies the MLR equation as below:

$$x1 + y2 + z3 + k4 = B0 + B1R + B2\beta + B3\alpha + \epsilon \quad (16)$$

This way, it is possible to isolate the individual forces, facilitating the determination of each propeller's thrust; hence, it clearly shows variation in motion types and orientations during drone flight and performance tests. To achieve this, the paper proposes four distinct drone flight tests on the test bed platform. These were achieved in roll, pitch, and yaw motions, each set in four distinct drone orientations, that is, in 90-degree variations, with the direction oriented towards load cell four (4) as the starting point. A visual representation of one such variant of these four separate tests is shown in Figure 11. From these four separate tests, the equation above becomes a four-system simultaneous equation (17) as below:

$$\begin{aligned} x1 + y2 + z3 + k4 &= B0 + B1R + B2\beta + B3\alpha + \epsilon \\ x1 + y2 + z3 + k4 &= B0 + B1R + B2\beta + B3\alpha + \epsilon \\ x1 + y2 + z3 + k4 &= B0 + B1R + B2\beta + B3\alpha + \epsilon \\ x1 + y2 + z3 + k4 &= B0 + B1R + B2\beta + B3\alpha + \epsilon \end{aligned} \quad (17)$$

The equation above yields x1, y2, z3, and k4, which, upon fitting into the set of equations (18) and (19) below, yield the thrust values of each respective propeller of a quadcopter:

$$\begin{aligned} P_{t1} &= x_1P_{t1} + y_2P_{t1} + z_3P_{t1} + k_4P_{t1} \\ P_{t2} &= x_1P_{t2} + y_2P_{t2} + z_3P_{t2} + k_4P_{t1} \\ P_{t3} &= x_1P_{t3} + y_2P_{t3} + z_3P_{t3} + k_4P_{t3} \\ P_{t4} &= x_1P_{t4} + y_2P_{t4} + z_3P_{t4} + k_4P_{t4} \end{aligned} \quad (18)$$

$$\begin{aligned} F_1 &= x_1P_{t1} + x_1P_{t2} + x_1P_{t3} + x_1P_{t4} \\ F_2 &= y_2P_{t1} + y_2P_{t2} + y_2P_{t3} + y_2P_{t4} \\ F_3 &= z_3P_{t1} + z_3P_{t2} + z_3P_{t3} + z_3P_{t4} \\ F_4 &= k_4P_{t1} + k_4P_{t2} + k_4P_{t3} + k_4P_{t4} \end{aligned} \quad (19)$$

Where F1, F2, F3, and F4 are force read from load cells 1, 2, 3, and 4 in each flight test; x1, y2, z3, and k4 are force percentage distributions to each load cell by the four propellers together; and Pt1, Pt2, Pt3, and Pt4 are thrust percentage contributions by each propeller to each load cell. It is important to note that equations (18) and (19) have a transpose relationship, as represented in equation (20):

$$F = (P_{ti})^T \quad (20)$$

The absolute error ±2.577 provides a direct measure of how far off a measurement is from its true value. In contrast, relative and percentage errors give context to that error in relation to the measurement's size.

4. Results and discussion

The resultant values were then analysed graphically (Figures 7 to 10). Tracking the contribution of each load cell with the varying loading points, a prediction model was developed capable of isolating resultant load cell force readings into respective individual propeller thrust values, irrespective of the quadcopter's orientation, position, or motion on the test bed. From this very collected data (training data), the model equation was developed.

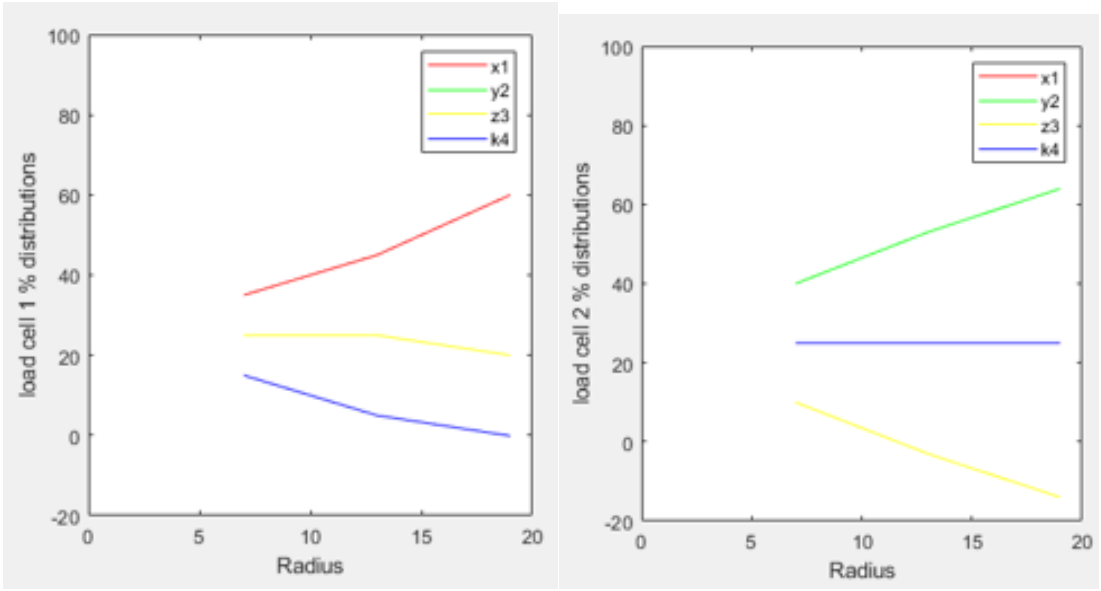

(a) **(b)**

Figure 7. Load cell weight distribution against predictor variables.

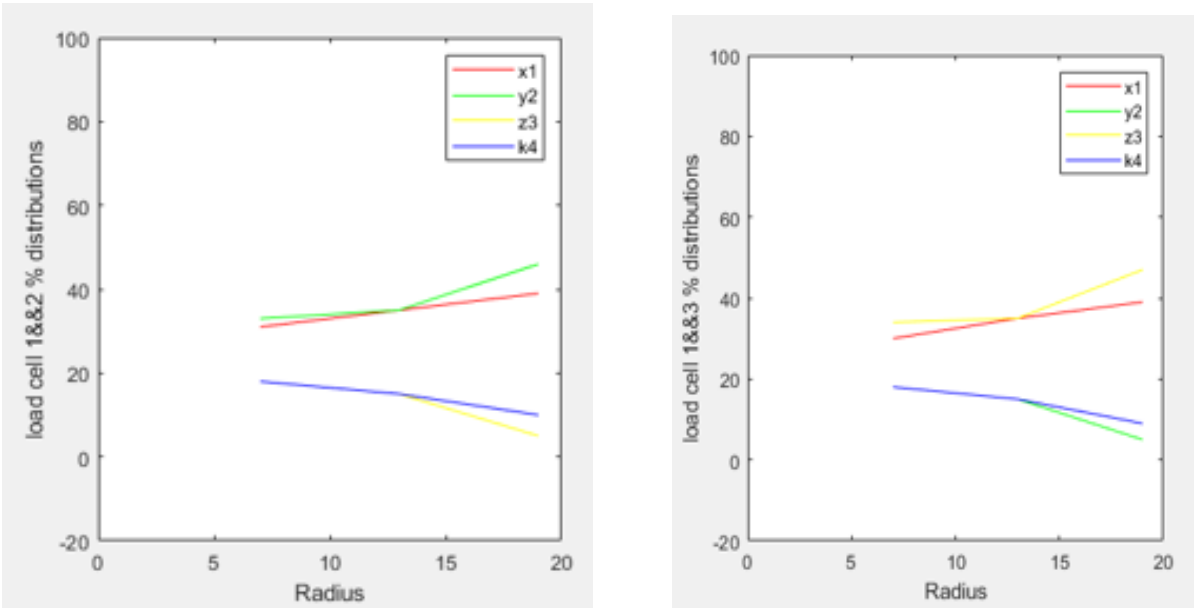

(c) **(d)**

Figure 8. Load cell weight distribution against predictor variables.

These figures (7 and 8) illustrate the relationship between radius and the percentage distribution of load across various directional components (x_1, y_2, z_3, and k_4) for four different load cell configurations. Each plot shows a distinct pattern of how these components contribute to the overall load distribution as the radius increases. In the first plot (top left), for example, the y and z components show an increasing trend with radius, while the x component decreases, and the k4 component

remains relatively stable. In the second plot (top right), the k component increases steadily with the radius. In contrast, the x component decreases, suggesting a shift in load distribution towards certain directions as the radius grows. The third plot (bottom left) shows similar trends, with the z component increasing and the x and y components decreasing as the radius expands, while k maintains a consistent contribution. In the fourth plot (bottom right), we again see z increasing with radius and x decreasing, with k remaining steady. Scientifically, these patterns suggest that load distribution varies with radius, indicating that certain directions or components become more dominant at larger distances from the centre. This insight is valuable for calibrating the force measurement system, as it helps to understand how load distribution shifts across different directions, allowing for more accurate modelling and prediction of forces at varying radial positions.

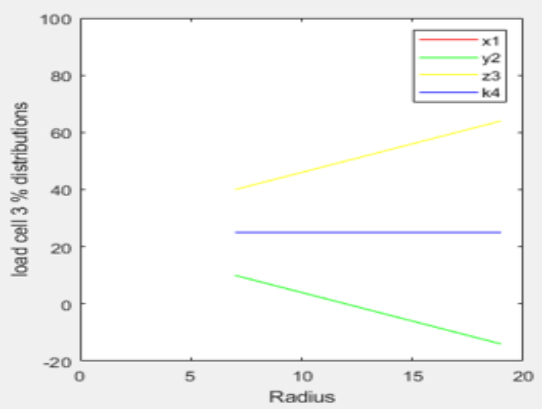

(e)

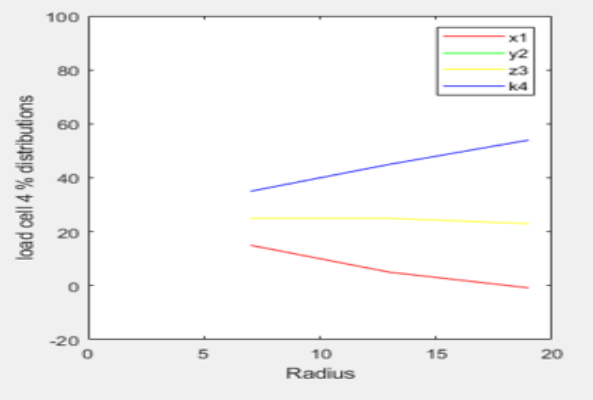

(f)

Figure 9. Load cell weight distribution against predictor variables

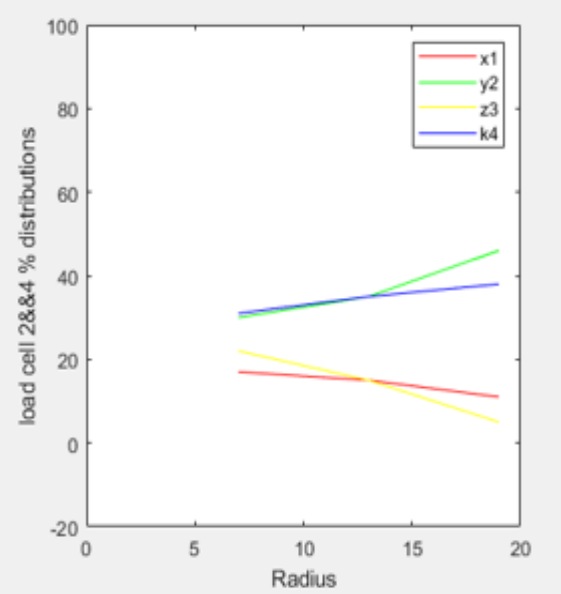

(g)

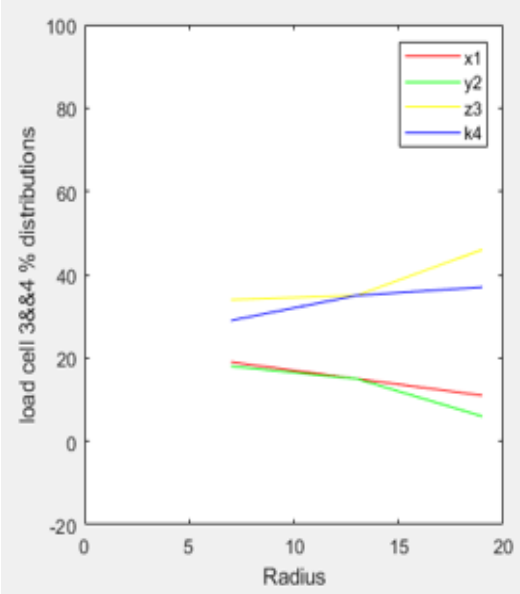

(h)

Figure 10. Load cell weight distribution against predictor variables

This figure presents four plots illustrating how the load distribution percentage across different directional components (x_1, y_2, z_3, and k_4) varies with radius for different load cell configurations. In general, the x and y components tend to increase as the radius grows, indicating that their contribution to the load distribution becomes more significant at greater distances. This trend suggests that these components are more sensitive to changes in radial position. Conversely, the z and k components

generally show a decreasing trend, particularly in the first, second, and fourth plots, implying that their influence diminishes with radius and that they may have a stronger effect closer to the centre. In some cases, such as k in the top-right plot, certain components remain relatively stable across the radius range, indicating a consistent influence. These trends provide insights into the spatial sensitivity of each load cell configuration, revealing how load distribution shifts across directions with radius. This information is valuable for accurately calibrating the force measurement system and predicting force variations at different distances, helping to create a reliable model of load distribution behaviour.

The justification for linearity and minimal correlation between predictor variables relies solely on the visual interpretation of graphs, which is insufficient. To validate these assumptions, a more rigorous statistical analysis, such as correlation coefficients, variance inflation factors, or residual diagnostics, is essential.

The multiple linear regression (MLR) equation was used to compute the respective thrust values. To obtain B0, B1, B2, and B_3 values, training data originally collected was compressed into percentage distributions across the four load cells for each loading point. The MLR model development lacks transparency. The process of compressing the data into percentage distributions is vague and could introduce biases.

From the respective summations, computation of the regression summations was possible through equations (5), (6), (7), (8), (9), (10), (11), (12), and (13), yielding set (21) below:

$$\sum(R)^2 = 576 \qquad \sum \beta Y = 784 \qquad (21)$$
$$\sum \alpha Y = 5.3 \qquad \sum(\beta)^2 = 867$$
$$\sum R\beta = 360 \qquad \sum(\alpha)^2 = 867$$
$$\sum R\alpha = 360 \qquad \sum RY = -5.4$$
$$\sum \beta\alpha = -291$$

With the regression sums computed, equation (14) was utilised in obtaining values of B_0,B_1, B_2, and B_3, yielding set (22) below:

B_0 = 47.75 (22)

B_1 = 3.819

B_2 = 3.091

B_3 = −2.77

Equation (3), therefore, evolves into equation (23) below to serve as the model equation fit to the drone testbed force measurement system:

$Y = 47.75 + 3.819R + 3.091 + 2.770\alpha$ (23)

The test data was then utilised to validate the above model equation and establish the presence (or absence) of an error. To achieve this, equation (3) was utilised by making the error, ϵ, the subject of the equation, thus yielding equation (24) below:

And equation (16) becomes:

$\epsilon = Y - B_0 - B_1R - B_2\beta - B_3\alpha$ (24)

By feeding the response variable Y (x_1, y_2, z_3, and k_4 values), intercept B_0, and predictor variables R, β, and α together with their respective coefficients B_1, B_2, and B_3, into equation (24), equation (25) below was obtained:

$\epsilon = Y - 47.75 - 3.819R - 3.091 - 2.770\alpha$ (25)

The test data (containing response and explanatory variables) was then utilised in equation (25) to test for error presence or absence. The presence of an error was eventually established to an average value of about ± 2.577, and equation (23), thus, becomes:

$$Y = 47.75 + 3.819R + 3.091\,\beta + 2.770\alpha \pm 2.577 \quad (26)$$

And equation set (17) becomes:

$$\begin{aligned} x1 + y1 + z1 + k_1 &= 47.75 + 3.819R + 3.091\,\beta + 2.770\alpha \pm 2.577 \\ x2 + y2 + z2 + k_2 &= 47.75 + 3.819R + 3.091\,\beta + 2.770\alpha \pm 2.577 \\ x3 + y3 + z3 + k_3 &= 47.75 + 3.819R + 3.091\,\beta + 2.770\alpha \pm 2.577 \\ x4 + y4 + z4 + k_4 &= 47.75 + 3.819R + 3.091\,\beta + 2.770\alpha \pm 2.577 \end{aligned} \quad (27)$$

The drone flight tests conducted (Figure 11), with propeller positions (radii, *R* and coordinates, and *α*) carefully noted, analogous to cases in Figures 6, 7, 8, 9, 210, and 11, facilitated the respective percentage contributions to the force sensors for each respective propeller. And with x_1, y_2, z_3, and k_4 successfully computed from equation set (25), it was possible to achieve this through the utilisation of the sets of equations (18), (19), and (20) by feeding into them the resultant x_1, y_2, z_3, and k_4 values obtained from equation set (27). The resultant computed force percentage distributions are as graphically represented in Figures (13 to 16).

Table 3. Response and Explanatory Variables

Loading Point	x_1	y_2	z_3	k_4	R	α	β
Σ	606.2 g	596 g	603 g	593.9 g	312 mm	192∘	192∘

Table 4. Response and Explanatory Variables Multiplied

Loading Point	X_1x_1	X_1y_2	X_1z_3	X_1k_4	X_2x_1	X_2y_2	X_2z_3	X_2k_4	X_3x_1	X_3y_2	X_3z_3	X_3k_4
Σ	7953.8 g	7730 g	7767 g	7732.1 g	4294.8 g	5904 g	4271 g	5507 g	5710 g	3650 g	5879 g	3959.1 g

Table 5. Response and Explanatory Variables Multiplied

Loading Point	$(X_1)^2$	$(X_2)^2$	$(X_3)^2$	X_1X_2	X_1X_3	X_2X_3
Σ	4632 g	2403 g	242063 g	2856 g	2856 g	1245 g

Drone flight tests were conducted to evaluate roll, pitch, and yaw motions, with each set performed in four different orientations of the drone, specifically at 90-degree intervals, starting with the direction facing load cell 4. The validation dataset consists of only four flight tests at these 90-degree intervals. To improve the robustness of the findings, additional tests should be conducted under varying weather conditions, with different payloads, and with various types of UAVs. Furthermore, extended durability testing, real-world scenario assessments, and high-performance manoeuvres should be included in future studies. Controlled tests for noise and vibration, along with cross-validation and independent site evaluations, can enhance the reliability of the results. A comprehensive uncertainty analysis that considers calibration, sensor precision, and environmental factors is essential for ensuring the broader applicability of the findings. A visual representation of one such variant is shown in Figure 11.

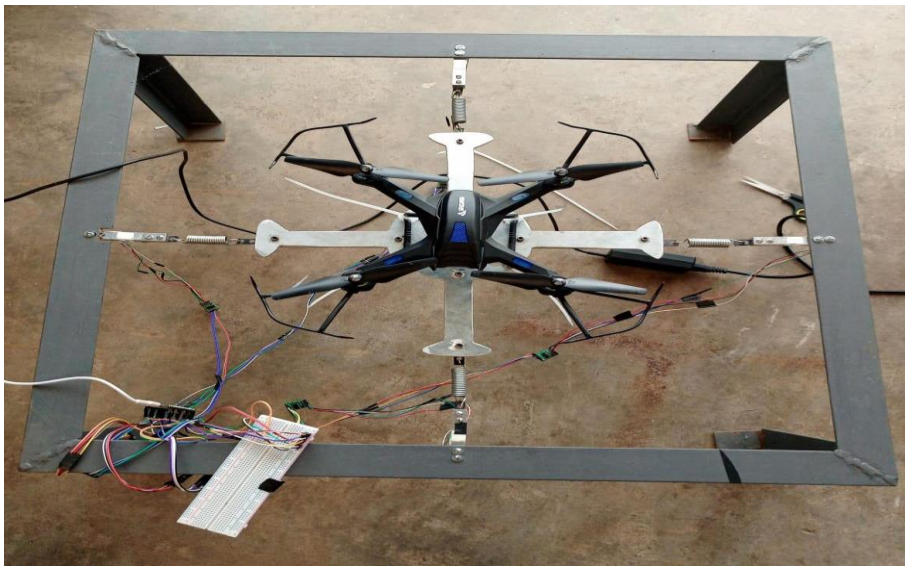

Figure 11. Drone Test Bed Performance Physical Flight Tests.

These respective tests yielded force distribution from the quadcopter's combined four propellers to the four force sensors. The distributions in thrust displayed in yaw (left and right), pitch (back and forth), and roll (left and right) are graphically represented in Figures 12 to 15.

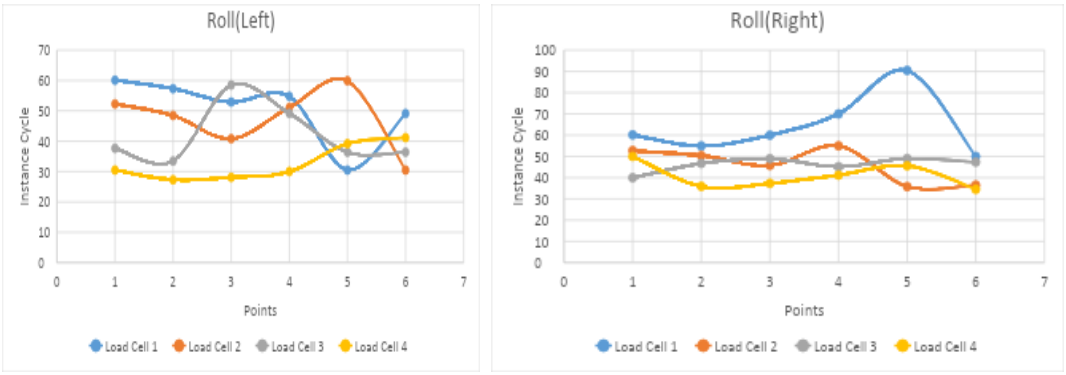

(a) (b)

Figure 11. Drone Flight Tests Force Distribution Graphs

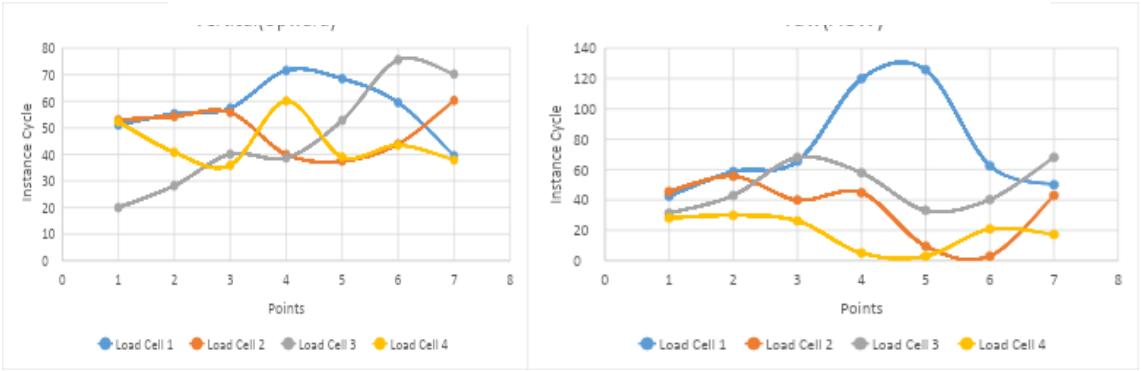

(c) (d)

Figure 13. Drone Flight Tests Force Distribution Graphs

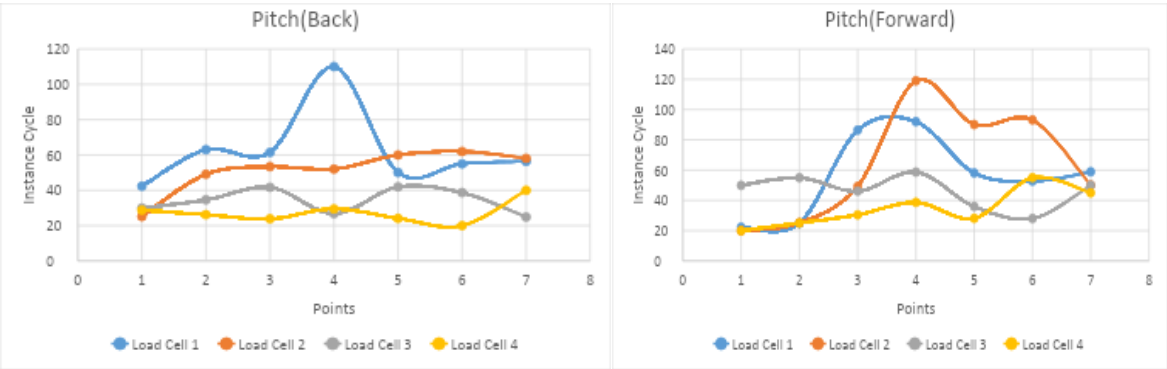

(e) (f)

Figure 14. Drone Flight Tests Force Distribution Graphs

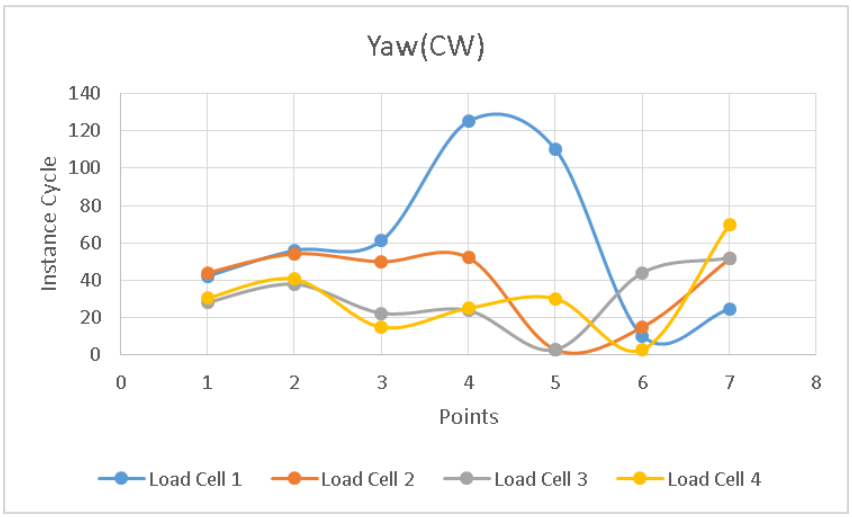

Figure 14. Drone Flight Tests Force Distribution Graphs

The Drone Flight Test Distribution Graphs in Figures 12 to 15 illustrate the force distribution across four load cells during various drone flight manoeuvres, including yaw, pitch, and roll motions. Ideally, the graphs should show a near-perfect linear distribution of forces across the load cells, reflecting the balanced thrust from the drone's propellers. However, deviations from this linearity are observed, likely due to mechanical vibrations between the drone and the test bed during flight. These deviations result in outliers, where certain load cells exhibit unexpected force spikes or drops. The inconsistencies suggest that while the system effectively captures thrust data, there are areas for improvement, particularly in mitigating vibrations and refining sensor accuracy. These enhancements reduce noise and provide more precise readings, improving the overall reliability of the system for future drone performance evaluations. An instance cycle is the concept of an instance cycle that refers to a virtual machine.

5. Conclusion

This paper primarily set out to realise a force measurement system capable of evaluating the directional forces of drones on the test bed through the isolation of a quadcopter's propeller thrusts from a four-crossed force sensor system. This entire process was achieved through initial design, development (physical fabrication), and repeated optimisation (through calibration) to realise a system of structural integrity and high force measurement precision. The mechanical design was achieved via Autodesk Inventor. Physical fabrication of the system was then subsequently achieved. This entailed mechanical fabrication of the frame and tension springs, electrical components (sensors and microcontroller) selection and installation, control and visual display

software, following synergistic integration of the modules into one system, and repeated system functionality tests allowed for smooth and efficient communication across the board. Calibration immediately followed in two phases. Phase 1 facilitated accurate force readings from the force sensors. Phase 2, on the other hand, provided training data, facilitating the development of model mathematical equations that catered for force (thrust) isolation. Subjection to test data from drone flight attached on the test bed, tests put the model equation at an error of ±2.577 (to quantify the impact of noise and vibrations on the reported accuracy of ±2.577 in my study, I can refer to relevant sections of discuss calibration, measurement procedures, and the behaviour of the system under test conditions. Findings on Noise and Vibrations are as follows:

1. Noise Contribution from Vibrations: Deviations from ideal linear distributions in the force sensor outputs were observed during drone flight tests. These were attributed to mechanical vibrations between the drone and the test bed, leading to force spikes or drops at individual sensors.

2. Calibration and error propagation), and capable of isolating/determining individual propeller thrusts, was thus achieved.

Acknowledgement

The authors would like to express their appreciation to the African Union and the Pan African University for Basic Sciences, Technology, and Innovation for providing financial support for this research.

References

[1] B, H.N.; Cowen, S. Radio-Tracking Wildlife with Drones : A Viewshed Analysis Quantifying Survey Coverage across Diverse Landscapes. 2019.

[2] Mesquita, G.P.; Mulero-pázmány, M.; Wich, S.A. A Practical Approach with Drones, Smartphones, and Tracking Tags for Potential Real-Time Animal Tracking. 2023, 208–214.

[3] Tansuriyavong, S.; Koja, H.; Kyan, M.; Anezaki, T. The Development of a Wildlife Tracking System Using Mobile Phone Communication Networks and Drones. 2018 International Conference on Intelligent Informatics and Biomedical Sciences, ICIIBMS 2018 2018, 3, 351–354, doi:10.1109/ICIIBMS.2018.8549936.

[4] Yavuz, D.; Akbıyık, H.; Bostancı, E. Intelligent Drone Navigation for Search and Rescue Operations. 2016, 565–568, doi:10.1109/siu.2016.7495803.

[5] Iob, P.; Frau, L.; Danieli, P.; Olivieri, L.; Bettanini, C. Avalanche Rescue with Autonomous Drones. 2020 IEEE International Workshop on Metrology for AeroSpace, MetroAeroSpace 2020 - Proceedings 2020, 319–324, doi:10.1109/MetroAeroSpace48742.2020.9160116.

[6] Avola, D.; Foresti, G.L.; Martinel, N.; Micheloni, C.; Pannone, D.; Piciarelli, C. Aerial Video Surveillance System for Small-Scale UAV Environment Monitoring. 2017 14th IEEE International Conference on Advanced Video and Signal Based Surveillance, AVSS 2017 2017, 0–5, doi:10.1109/AVSS.2017.8078523.

[7] Burkert, F.; Fraundorfer, F. Uav-Based Monitoring of Pedestrian Groups. The International Archives of the Photogrammetry, Remote Sensing and Spatial Information Sciences 2013, XL-1/W2, 67–72, doi:10.5194/isprsarchives-xl-1-w2-67-2013.

[8] Grote, M.; Cherrett, T.; Oakey, A.; Royall, P.G.; Whalley, S.; Dickinson, J. How Do Dangerous Goods Regulations Apply to Uncrewed Aerial Vehicles Transporting Medical Cargos? Drones 2021, 5, 1–24, doi:10.3390/drones5020038.

[9] Escribano Macias, J.; Angeloudis, P.; Ochieng, W. Optimal Hub Selection for Rapid Medical Deliveries Using Unmanned Aerial Vehicles. Transp Res Part C Emerg Technol 2020, 110, 56–80, doi:10.1016/j.trc.2019.11.002.

[10] Magnetometer, F. Indoor Mapping of Magnetic Fields Using UAV Equipped With. 2021.

[11] Yaprak, S.; Yildirim, Ö.; Susam, T. UAV Based Agricultural Planning and Landslide Monitoring. TeMA Journal of Land Use Mobility and Environment 2017, 3, 325–338.

[12] Barnawi, A.; Chhikara, P.; Tekchandani, R.; Kumar, N.; Alzahrani, B. Artificial Intelligence-Enabled Internet of Things-Based System for

COVID-19 Screening Using Aerial Thermal Imaging. Future Generation Computer Systems 2021, 124, 119–132, doi:10.1016/j.future.2021.05.019.

[13] Aktas, Y.O.; Ozdemir, U.; Dereli, Y.; Tarhan, A.F.; Cetin, A.; Vuruskan, A.; Yuksek, B.; Cengiz, H.; Basdemir, S.; Ucar, M.; et al. A Low Cost Prototyping Approach for Design Analysis and Flight Testing of the TURAC VTOL UAV. 2014 International Conference on Unmanned Aircraft Systems, ICUAS 2014 - Conference Proceedings 2014, 1029–1039, doi:10.1109/ICUAS.2014.6842354.

[14] Gefang, W.; Ning, H.; Yanmei, L.; Dong, Z. UAV Onboard Electronic Detection System Based on Simulation Test Technology. 2013.

[15] Bo, P.; M, A.A.A.; Blis, P.; N, I.I. Navigation Control and Stability Investigation of a Mobile Robot Based on a Hexacopter Equipped with an Integrated Manipulator. 2017, 1–13, doi:10.1177/1729881417738103.

[16] Braun, J.; Braunová, H.; Suk, T.; Ovský, P.P.E.Ť.; Kuric, I. Structural and Geometrical Vegetation Filtering - Case Study on Mining Area Point Cloud Acquired by UAV Lidar. 2021, 26.

[17] Huang, R. TigerPrints Design and Demonstration of a Two-Dimensional Test Bed for UAV Controller Evaluation; 2014;

[18] Huang, R. TigerPrints Design and Demonstration of a Two-Dimentional Test Bed for UAV Controller Evaluation Design and Demonstration of a Two-Dimensional Test Bed for UAV Controller Evaluation. 2014.

[19] Pounds, P.E.I.; Bersak, D.R.; Dollar, A.M. Grasping from the Air: Hovering Capture and Load Stability. Proc IEEE Int Conf Robot Autom 2011, 2491–2498, doi:10.1109/ICRA.2011.5980314.

[20] Danko, T.W.; Oh, P.Y. A Hyper-Redundant Manipulator for Mobile Manipulating Unmanned Aerial Vehicles. 2013.

[21] Valiga, M.; Novotnák, J.; Šmelko, M.; Cekanová, A.; Košuda, M. Control System Design of UAV Starter-Generator Power Unit. NTinAD 2019 - New Trends in Aviation Development 2019 - 14th International Scientific Conference, Proceedings 2019, 204–208, doi:10.1109/NTAD.2019.8875608.

[22] Bendea, H.; Boccardo, P.; Dequal, S.; Tonolo, F.G.; Marenchino, D.; Piras, M.; Torino, P. LOW COST UAV FOR POST-DISASTER ASSESSMENT. 1373–1380.

[23] Valencia, E. Weight and Performance Methodology of a UAV at Cruise Condition for Precision Agriculture. 2017, 1–15, doi:10.2514/6.2017-4868.

[24] Muthusamy, P.K.; Garratt, M.; Pota, H.R.; Kok, J.M. Bidirectional Fuzzy Brain Emotional Learning Control for Aerial Robots. 2018, doi:10.1109/SSCI.2018.8628809.

[25] Novotňák, J.; Fiľko, M.; Lipovský, P.; Šmelko, M. Design of the System for Measuring UAV Parameters. Drones 2022, 6, doi:10.3390/drones6080213.

[26] Futek Certification: Why Is It Important to Calibrate Load Cell and Torque Sensors?

[27] Qu, J.; Member, S.; Wu, Q.; Member, S.; Clancy, T.; Fan, Q. 3D-Printed Strain-Gauge Micro Force Sensors. 2020, 1748, 1–8, doi:10.1109/JSEN.2020.2976508.

[28] Random Nerd Tutorials Arduino with Load Cell and HX711 Amplifier (Digital Scale).

[29] Adam Hayes, D.K.T.L. Multiple Linear Regression (MLR) Definition, Formula, and Example.

[30] Mingtai, C. Static Thrust Measurement for Propeller-Driven Light Aircraft;